Simulation of NMR spectra at zero- and ultra-low field from A to Z – a tribute to Prof. Konstantin L'vovich Ivanov

Quentin Stern[1], Kirill Sheberstov[2]

[1]Univ Lyon, CNRS, ENS Lyon, UCBL, Université de Lyon, CRMN UMR 5280, 69100 Villeurbanne, France
5 [2]Laboratoire des biomolécules, LBM, Département de chimie, École normale supérieure, PSL University, Sorbonne Université, CNRS, 75005 Paris, France

Correspondence to: Quentin Stern (quentin.stern@protonmail.com)

Abstract. Simulating NMR experiments may appear mysterious and even daunting for those who are new to the field. Yet, broken down into pieces, the process may turn out to be easier than expected. Quite to the opposite, it is in fact a powerful
10 and playful means to get insights into the spin dynamics of NMR experiments. In this Tutorial Paper, we show step by step how some NMR experiments can be simulated, assuming as little prior knowledge from the reader as possible. We focus on the case of NMR at zero- and ultra-low field, an emerging modality of NMR in which the spin dynamics is dominated by spin-spin interactions rather than spin-field interactions, as is usually the case of conventional high-field NMR. We first show how to simulate spectra numerically. In a second step, we detail an approach to construct an eigenbasis for systems of
15 spin-½ nuclei at zero-field. We then use it to interpret the numerical simulations. In this attempt to make NMR simulation approachable, the authors wish to pay a tribute to Prof. Konstantin L'vovich Ivanov, a great scientist and pedagogue who passed away on March 5th 2021.

1 Introduction

NMR spectroscopists know well the advantages of performing experiments at the highest possible magnetic field. Increasing
20 magnetic field strength boosts the sensitivity thanks to higher Boltzmann nuclear polarization and higher Larmor frequency. In addition to this already convincing advantage, higher magnetic fields also imply larger chemical shift dispersion and therefore easier resolution of individual resonances in crowded spectra. This has motivated the use of ever-increasing magnetic fields. The past year has witnessed the implementation of the first spectrometers operating at no less than 28 T, corresponding to a ¹H Larmor frequency of 1.2 GHz (Schwalbe, 2017; Thayer and Pines, 1987). There is no doubt these
25 new instruments will allow for unprecedented applications.

On the fringe of these great achievements, growing interest is going to an opposite strategy, namely, zero- to ultralow-field NMR (ZULF), a modality of NMR experiments where the dominant interactions are spin-spin rather than spin-field interactions (Thayer and Pines, 1987; Weitekamp et al., 1983; Blanchard and Budker, 2016; Blanchard et al., 2021; Tayler et al., 2017). To realize such condition, ZULF experiments are not performed in magnets but rather in μ-metal magnetic shields
30 which screen magnetic fields originating from the Earth and other surrounding sources, bringing the residual field down to

nT values. 'Zero-field' (ZF) usually designates the regime where the magnetic field is so low that it does no longer influence the outcome of the experiment while ultra-low field (ULF) designates the regime where the Zeeman interaction (spin-field) can be treated as a perturbation to the spin-spin interactions. Liquid-state ZULF experiment therefore result in J-spectra which do not feature any chemical shift information(Ledbetter et al., 2009). In the simplest form of ZULF experiments, the

35   sample is thermally prepolarized in a permanent magnet (typically 2 T) (Tayler et al., 2017) and subsequently shuttled into the magnetic shields for detection at ZF or ULF. Alternatively, ZULF experiments may be coupled with hyperpolarization techniques (Theis et al., 2012; Butler et al., 2013b; Barskiy et al., 2019). In particular, parahydrogen induced polarization (PHIP) has become common as a method for enhancing ZULF signal (Theis et al., 2012; Butler et al., 2013b). Once the sample is prepolarized (or hyperpolarized), coherences are excited using constant magnetic field pulses rather than

40   radiofrequency (RF) pulses and are usually detected using optically pumped magnetometers (OPM) rather than inductive coils. Contrary to high-field instruments, ZULF spectrometers have the advantage of being cheap and relatively easy to assemble (Tayler et al., 2017). They are small enough to sit on a bench and do not require the use of cryogenics (at least if OPMs are used for detection).

Most people who have been introduced to the theory of high-field NMR have first encountered the vector model. This simple

45   idealization of a single spin system as a vector in 3D-space is a powerful tool to build intuition on what happens during an NMR experiment. Then, in a second step, the product operator formalism is necessary to understand the outcome of experiments involving interacting spins. At ZULF, there is no such intuition as the vector model. The simplest ZULF experiment consists of detecting the coherence between the singlet S_0 and triplet T_0 states of a pair of J-coupled heteronuclei, e.g. ^{1}H and ^{13}C (Blanchard and Budker, 2016). Polarization oscillates back and forth from one of the heteronucleus to the

50   other, producing an observable oscillating signal, whose frequency is given by the J-coupling between the two spins. The outcome of the experiment is simple – a single line at the J-coupling frequency – although it cannot be predicted by a simple vector model and Bloch equations. Nonetheless, it is possible to build intuition regarding ZULF experiments in several ways. First, when dealing with two-spin systems, one can define spin operators at ZF in analogy to that at high-field so as to translate some of the intuitions from high-field to ZULF (Blanchard and Budker, 2016; Butler et al., 2013b). Second, there is

55   a strong analogy between the energy states of electronic spins in atoms and coupled nuclei at ZF (Butler et al., 2013a; Theis et al., 2013). The formalism of atomic physics can therefore be used to describe ZULF experiments. Finally, ZULF experiments can easily be numerically simulated and – as is the case for high-field NMR – simulation provides a playful means to understand NMR experiments (Blanchard et al., 2020; Put et al., 2021). This tutorial paper is focused on the last two approaches.

60   We present a step-by-step procedure to numerically simulate ZULF spectra in some simple cases. The process is broken down into the following steps:

1. Define the experimental sequence
2. Define the spin system
3. Compute the spin Hamiltonian

4. Define the initial state: compute the initial density matrix

5. Propagate the density matrix under the Hamiltonians

6. Extract expectation values from the propagation

7. Fourier transform the expectation values to obtain a spectrum

We assume that the reader is familiar with general concepts of NMR but not necessarily with simulation. We take particular care to detail the technical "tricks" which are generally omitted in research papers but are nonetheless essential to perform successful simulations. We present simulated spectra for XA_n spin systems with n between 1 and 5 with several excitation schemes. The spectra are simulated using MATLAB live scripts which are available in the Supplementary Material. The code is abundantly commented and is constructed so as to follow precisely the recipe presented in this Paper. Each object and operation presented in this Paper can thus be related to lines in the MATLAB code, and vice versa. PDF version of the live scripts are available. We strongly advise the reader to read the code in parallel to the Paper.

In a second step, we interpret the simulated results by performing an analytical analysis of XA_n system using a theoretical framework coming from atomic physics. We show how to construct an eigenbasis and find the selection rules for the allowed transitions.

The reader might wonder whether it makes sense to go through all the details of simulating NMR experiments from scratch while there are powerful simulation packages, which are freely available. *SpinDynamica* (Bengs and Levitt, 2018) and Spinach (Hogben et al., 2011), which run on Mathematica and MATLAB, respectively, are probably the most appropriate tools for simulations at ZULF and the people who have programmed these have already gone through the hurdles of making them efficient and versatile for us. However, it is the Authors' opinion that performing simple simulations from scratch is the best way to get familiar with the quantum mechanical objects of NMR theory. Once one is confident with these objects and their language, one will make the best use of powerful packages such as *SpinDynamica* and Spinach.

In writing this Paper, the Authors wish to pay a tribute to their regretted lecturer and mentor Prof. Kostantin L'vovich Ivanov, known as Kostya by many, who was taken by COVID-19 on March 5th 2021 (Yurkovskaya and Bodenhausen, 2021). KS had KI as PhD co-supervisor performing research on long-lived states, parahydrogen induced polarization, and chemically induced dynamic nuclear polarization (CIDNP). KI's deep understanding of underlying physics allowed his group to work in very different directions, for example to combine CIDNP and ZULF NMR. During his PhD in Sami Jannin's team in Lyon, France, QS collaborated with KI on a research project. In the course of their collaboration, KI gave QS guidance on how to simulate experiments at ZF. A few advices turned into precious teachings for QS. Sadly, these teachings were brutally interrupted by KI's death. KI's kindness and availability to give help and advice will ever remain an example for QS and KS.

2 Theory – numerical simulation of spin dynamics

95

2.1 Define the experimental sequence

Most 1D NMR experiments can be broken down into three steps:

preparation – mixing – detection

During the preparation, some nuclear polarization is acquired by letting the sample rest in a strong magnetic field (in most
100 conventional experiments). Mixing consists of bringing the system to a non-stationary state whose oscillations are recorded
during detection. In common high-field NMR experiments, all the steps are performed in a strong magnet with a nearly
constant magnetic field. Nuclear polarization is spontaneously acquired due to the high magnetic field and both the mixing
and detection are performed through the same RF coil using Faraday induction. At ZULF, there is no nuclear polarization so
the preparation has to be performed in different conditions. A common method is to shuttle the sample between a region of
105 high-field and a region of ZULF.

Figure 1 shows a typical experimental setup. A permanent magnet is used to prepolarize the sample and is connected with
the magnetic shields by a guiding solenoid coil. This coil ensures that the sample experiences a magnetic field with constant
direction and sufficient strength during the transfer from the region of high-field to inside the magnetic shields (i.e. the coil
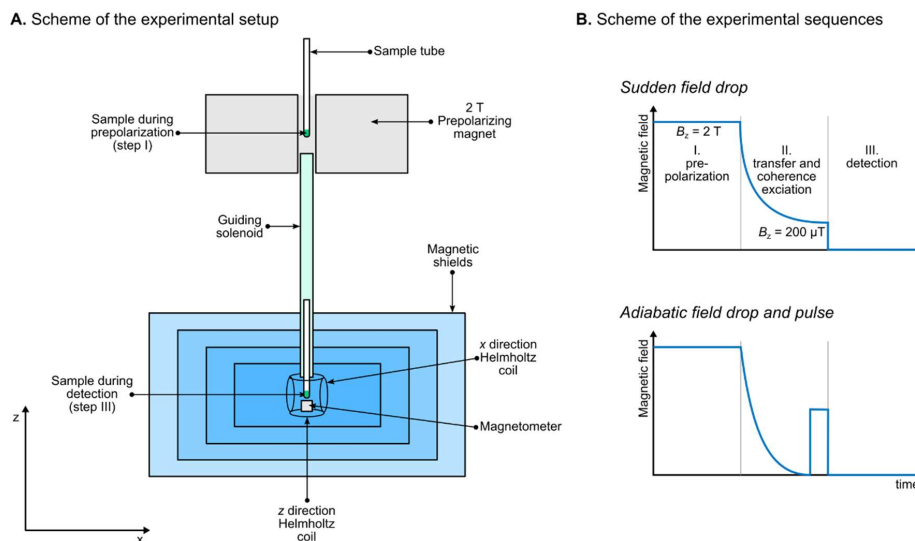
**Figure 1: A. Typical experimental setup for ZULF experiments. Note that the sample is represented in two places on the same
drawing even if there is a single sample. B. Schemes of the experimental sequences for measurements at ZF using a sudden field
drop or an adiabatic field drop followed by a pulse of static magnetic field.**

ensures an adiabatic transfer). Once the sample arrives in the magnetic shields at the location of detection, the Helmholtz coil

110 continues to produce a magnetic field in the same direction as the solenoid and the spin system is still distributed into Zeeman populations (Blanchard and Budker, 2016; Tayler et al., 2017). All the steps detailed until here are part of the preparation. In practice, the guiding solenoid and the Helmoltz coil produce a magnetic field which is much weaker than the prepolarizing magnet. However, this will not be taken into account in the simulation: we consider that the sample spends enough time in the prepolarizing magnet to reach Boltzmann equilibrium and that the transfer is sufficiently fast for us to

115 neglect the change in polarization during the transfer.

A further step can optionally be added to the preparation which consists of ramping down the magnetic field produced by the Helmholtz coil to bring the spins adiabatically to ZF. We will refer to experiments which include or do not include this step as the adiabatic field drop and sudden field drop experiments, respectively. In the case of sudden field drop experiments, the mixing step simply consists of switching off the magnetic field non-adiabatically (that is, fast enough to be considered

120 instantaneous with respect to the evolution of the spin system). In the case of adiabatic field drop experiments, the sample is already at ZF at the end of preparation and so populations have to be mixed by applying a magnetic field pulse, before any signal can be detected. This is analogous to high-field pulses except that it uses constant magnetic field rather than RF pulses. After the mixing, the oscillating magnetic field generated by the sample is detected by an optical magnetometer. In Fig. 1, the magnetometer is represented below the sample, that is, aligned along the z-axis with respect to the sample. We

125 assume that the OPM is configured so as to be sensitive to magnetic field along the z-axis. During detection, a weak magnetic field may be applied, either along the z-axis or along an orthogonal axis. In the latter case, the experiment is said to be performed under ULF regime. In absence of applied magnetic field (and provided the residual magnetic field is properly zeroed at the location of the sample), the experiment is said to be performed under ZF regime.

In summary, there are several possible combinations of experimental schemes. All of them start with prepolarizing the spins

130 at high magnetic field. After the sample is transported into the magnetic shields, the field is dropped either suddenly or adiabatically, in which case a magnetic field pulse is applied. Finally, the oscillating magnetic field produced by the sample is detected along the z-axis, with or without a weak magnetic field applied the x-axis. In the remaining of the paper, these sequences presented in Figure 2 will be broken down into the following steps:

1. Pre-polarization

135 2. Transfer and coherence excitation

3. Detection

2.2 Define the spin system

This step consists of listing the different magnetic sites of the molecule whose ZULF spectrum is to be simulated and the interactions which the spins are subject to. This paper is concerned with small molecules in the liquid state. As is the case for

140 high-field NMR, dipolar interactions are averaged out by rapid molecular tumbling and need not to be taken into account

(except as stochastic perturbation if one intends to include relaxation effects). Therefore, only the *J*-coupling and the Zeeman interactions are considered here.

In this Paper, we consider spin systems of the form XA_n, where X is a ^{13}C spin coupled to n equivalent ^1H spins A through a coupling J_{AX}. A spins are coupled together through J_{AA}.

145 **2.3 Compute the spin Hamiltonian**

The Hamiltonian is the operator which represents the energy of the system. Information about the spin system is mathematically encoded in the spin Hamiltonian. We will first present how the Hamiltonian for the Zeeman interaction of a single spin is computed based on Pauli matrices. Then, we will present the construction of a two-spin system using the Kronecker product of individual spin spaces to compute the Zeeman and the *J*-coupling Hamiltonians. Finally, we will show

150 how the procedure is extended to an arbitrary number of spins.

Let us first assume that the system contains a single spin-1/2 interacting with the magnetic field $\boldsymbol{B}$, which we assume to be along the z-axis. We chose to represent the spin system in the Zeeman basis

$$\mathcal{B}_Z^2 = \{|\alpha\rangle, |\beta\rangle\}. \tag{1}$$

where the superscript indicates the size of the Hilbert space. The α and β states correspond to the spin being parallel and

155 antiparallel with the magnetic field, respectively. Note that the choice of the Zeeman basis is convenient for numerical simulation but it not necessary. The general state in which the spin may be found is a linear combination of these two basis states.

The angular momentum of a single spin is associated with the spin angular momentum operators, which can be represented as a vector along each Cartesian coordinate

160 $$\hat{\boldsymbol{I}} = \begin{pmatrix} \hat{I}_x & \hat{I}_y & \hat{I}_z \end{pmatrix}. \tag{2}$$

These operators act on the Zeeman states in certain ways, e.g. $\hat{I}_x|\alpha\rangle = \frac{1}{2}|\beta\rangle$. To summarize the set of rules it is convenient to use matrices, with the matrix elements determined by the action of the operator on the α and β states: $\hat{I}_k^{ij} = \langle j|\hat{I}_k|i\rangle$, where $i, j \in \{\alpha, \beta\}; k \in \{x, y, z\}$. These matrices are proportional to Pauli matrices $\hat{\sigma}_x$, $\hat{\sigma}_y$ and $\hat{\sigma}_z$

$$\begin{aligned} \hat{I}_x &= \frac{1}{2}\hat{\sigma}_x = \frac{1}{2}\begin{pmatrix} 0 & 1 \\ 1 & 0 \end{pmatrix} \\ \hat{I}_y &= \frac{1}{2}\hat{\sigma}_y = \frac{1}{2}\begin{pmatrix} 0 & -i \\ i & 0 \end{pmatrix}. \\ \hat{I}_z &= \frac{1}{2}\hat{\sigma}_z = \frac{1}{2}\begin{pmatrix} 1 & 0 \\ 0 & -1 \end{pmatrix} \end{aligned} \tag{3}$$

165 The interaction of a single spin with a magnetic field $\boldsymbol{B}$ is given by the Zeeman Hamiltonian

$$\hat{H}_Z = -\gamma \boldsymbol{B} \cdot \hat{\boldsymbol{I}} = -\gamma \left(B_x \hat{I}_x + B_y \hat{I}_y + B_z \hat{I}_z \right), \tag{4}$$

where γ is the gyromagnetic ratio of the spin. The dot product of the vectors of the magnetic field and of the spin angular momentum is expanded on the right member of (4). Note that we have omitted the reduced Planck constant $\hbar$ in (4), which implies that the energy is expressed in rad.s^{-1} rather than in Joules. This is the case throughout this Paper. In many cases, the

170 magnetic field is aligned with one of the axes. If it points along the z-axis, $i.e.$, $\boldsymbol{B} = (0 \quad 0 \quad B_0)$, (4) simplifies to

$$\hat{H}_Z = -\gamma B_0 \hat{I}_z = \omega^0 \hat{I}_z = \frac{1}{2}\begin{pmatrix} +\omega^0 & 0 \\ 0 & -\omega^0 \end{pmatrix}, \qquad (5)$$

where $\omega^0 = -\gamma B_0$ is the Larmor frequency of the spin.

The single spin whose Hamiltonian is given by (5) lives in a Hilbert space of dimension 2. To represent a pair of spins 1/2, we need to use a Hilbert space with a dimension of 4. To do so, we redefine the angular momentum operators in this higher

175 dimensional space. The angular momentum operators $\hat{I}_{1x}$, $\hat{I}_{1y}$ and $\hat{I}_{1z}$ and $\hat{I}_{2x}$, $\hat{I}_{2y}$ and $\hat{I}_{2z}$ of spin 1 and spin 2, respectively, are given by the Kronecker product of single-spin angular momentum operator and the identity operator, in the appropriate order. For the z-axis angular momentum operators, we have

$$\hat{I}_{1z} = \hat{I}_z \otimes \hat{1} = \frac{1}{2}\begin{pmatrix} 1 & 0 \\ 0 & -1 \end{pmatrix} \otimes \begin{pmatrix} 1 & 0 \\ 0 & 1 \end{pmatrix} = \frac{1}{2}\begin{pmatrix} +1 & 0 & 0 & 0 \\ 0 & +1 & 0 & 0 \\ 0 & 0 & -1 & 0 \\ 0 & 0 & 0 & -1 \end{pmatrix} \qquad (6)$$

and

180 $$\hat{I}_{2z} = \hat{1} \otimes \hat{I}_z = \begin{pmatrix} 1 & 0 \\ 0 & 1 \end{pmatrix} \otimes \frac{1}{2}\begin{pmatrix} 1 & 0 \\ 0 & -1 \end{pmatrix} = \frac{1}{2}\begin{pmatrix} +1 & 0 & 0 & 0 \\ 0 & -1 & 0 & 0 \\ 0 & 0 & +1 & 0 \\ 0 & 0 & 0 & -1 \end{pmatrix}. \qquad (7)$$

Similar expressions are obtained for x and y operators. They are not shown here but are available in many textbooks (Hore et al., 2015; Levitt, 2013). Here we have used the following convention for the Kronecker product:

$$\begin{pmatrix} a & b \\ c & d \end{pmatrix} \otimes \begin{pmatrix} \alpha & \beta \\ \gamma & \delta \end{pmatrix} = \begin{pmatrix} a\begin{pmatrix} \alpha & \beta \\ \gamma & \delta \end{pmatrix} & b\begin{pmatrix} \alpha & \beta \\ \gamma & \delta \end{pmatrix} \\ c\begin{pmatrix} \alpha & \beta \\ \gamma & \delta \end{pmatrix} & d\begin{pmatrix} \alpha & \beta \\ \gamma & \delta \end{pmatrix} \end{pmatrix} = \begin{pmatrix} a\alpha & a\beta & b\alpha & b\beta \\ a\gamma & a\delta & b\gamma & b\delta \\ c\alpha & c\beta & d\alpha & d\beta \\ c\gamma & c\delta & d\gamma & d\delta \end{pmatrix}, \qquad (8)$$

The two operators defined by (6) and (7) are the same as the one given by (5), except that the world of spin 1 now contains

185 spin 2, and vice versa. This representation corresponds to a basis which is the Kronecker product of the basis of the individual spins

$$\mathcal{B}_Z^4 = \mathcal{B}_Z^2 \otimes \mathcal{B}_Z^2 = \{|\alpha\alpha\rangle, |\alpha\beta\rangle, |\beta\alpha\rangle, |\beta\beta\rangle\}. \qquad (9)$$

For the case where the magnetic field points along the z-axis, the total Zeeman Hamiltonian for the two spins can now be computed using (5) in the basis of (9) as the sum of the two Zeeman Hamiltonians:

190 $\hat{H}_Z = \hat{H}_{Z,1} + \hat{H}_{Z,2} = \omega_1^0 \hat{I}_{1z} + \omega_2^0 \hat{I}_{2z} = \frac{1}{2} \begin{pmatrix} +\omega_1^0 + \omega_2^0 & 0 & 0 & 0 \\ 0 & +\omega_1^0 - \omega_2^0 & 0 & 0 \\ 0 & 0 & -\omega_1^0 + \omega_2^0 & 0 \\ 0 & 0 & 0 & -\omega_1^0 - \omega_2^0 \end{pmatrix},$ (10)

where ω_1^0 and ω_2^0 are the Larmor frequencies of spin 1 and 2, respectively. Note that in a Hilbert space of several spin, it is useful to define projections of total angular momentum operators

$$\hat{I}_x = \hat{I}_{1x} + \hat{I}_{2x}$$

$$\hat{I}_y = \hat{I}_{1y} + \hat{I}_{2y}.$$ (11)

195 $\hat{I}_z = \hat{I}_{1z} + \hat{I}_{2z}$

At this point, the two spins are represented in a common space but they do not interact. The J-coupling Hamiltonian for the pair of spins is given by

$$\hat{H}_J = 2\pi J \hat{\boldsymbol{I}}_1 \cdot \hat{\boldsymbol{I}}_2 = 2\pi J (\hat{I}_{1x} \hat{I}_{2x} + \hat{I}_{1y} \hat{I}_{2y} + \hat{I}_{1z} \hat{I}_{2z}) = \pi J \begin{pmatrix} 1/2 & 0 & 0 & 0 \\ 0 & -1/2 & 1 & 0 \\ 0 & 1 & -1/2 & 0 \\ 0 & 0 & 0 & 1/2 \end{pmatrix},$$ (12)

where J is the J-coupling between the two spins in Hz. Compared with the Zeeman Hamiltonian (see (10)), the J-coupling

200 Hamiltonian has the particularity to have off-diagonal elements in the $\{|\alpha\beta\rangle, |\beta\alpha\rangle\}$ subspace, which implies that the J-interaction mixes the $|\alpha\beta\rangle$ and $|\beta\alpha\rangle$ states. In other words, due to the J-interaction, these two states are no longer eigenstates of the spin system.

In the case of a system of n spins, the same procedure can be applied to define the angular momentum operators and the Hamiltonians. These operators can be represented as $2^n \times 2^n$ matrices. (6) and (7) generalize to

205 $\hat{I}_{kz} = \otimes_{l=1}^n \hat{u}_{z,l}$ where $\hat{u}_{z,l} = \begin{cases} \hat{1} \text{ if } l \neq k \\ \hat{I}_z \text{ if } l = k' \end{cases}$ (13)

where $\hat{1}$ and $\hat{I}_{kz}$ are the identity operator and the z-angular momentum operator of spin k in an n-spin space and $\hat{u}_{z,l}$ operators are defined in a single-spin space. The z-projection of total angular momentum operators is given by

$$\hat{I}_z = \sum_{l=1}^n \hat{I}_{lz}.$$ (14)

(13) and (14) are shown for z operators but apply similarly for x and y operators. The Zeeman Hamiltonian for a system of n

210 spins is given by

$$\hat{H}_Z = -\sum_{l=1}^n \gamma_l \boldsymbol{B} \cdot \hat{\boldsymbol{I}}_l = -\sum_{l=1}^n \gamma_l (B_x \hat{I}_{lx} + B_y \hat{I}_{ly} + B_z \hat{I}_{lz}).$$ (15)

where γ_l is the gyromagnetic ratio of spin l. The J-Hamiltonian in the same space is given by

$$\hat{H}_J = 2\pi \sum_{l>k}^{n} J_{lk} \hat{\boldsymbol{I}}_l \cdot \hat{\boldsymbol{I}}_k = 2\pi \sum_{l>k}^{n} J_{lk} \left(\hat{I}_{lx}\hat{I}_{kx} + \hat{I}_{ly}\hat{I}_{ky} + \hat{I}_{lz}\hat{I}_{kz} \right), \tag{16}$$

where J_{lk} is the J-coupling between spins l and k in Hz. Because a spin is not J-coupled to itself, the sum in (16) does not
215 include terms with $l = k$. Furthermore, to avoid counting terms twice, terms with $l < k$ are not included either, leaving only $l > k$ terms.

2.4 Define the initial state: compute the initial density matrix

The state of a spin system during an NMR experiment is described by a density operator. If $|\psi\rangle$ is a ket representing the state of the system as a linear combination of basis states (as defined in (1) and (9)), the density operator is given by

220 $$\hat{\rho} = \overline{|\psi\rangle\langle\psi|}. \tag{17}$$

The upper bar on (17) represents the ensemble average over all identical spin systems in the sample. This averaging makes the density operator formalism well-suited for NMR where the experiment consists of observing a large number of identical spin systems at the same time, rather than a single spin system. For example, the matrix representation of the density operator for the α and β states of a single spin yields

225 $$\hat{\rho}_\alpha = \overline{|\alpha\rangle\langle\alpha|} = \begin{pmatrix} 1 \\ 0 \end{pmatrix}(1 \quad 0) = \begin{pmatrix} 1 & 0 \\ 0 & 0 \end{pmatrix}$$
$$\hat{\rho}_\beta = \overline{|\beta\rangle\langle\beta|} = \begin{pmatrix} 0 \\ 1 \end{pmatrix}(0 \quad 1) = \begin{pmatrix} 0 & 0 \\ 0 & 1 \end{pmatrix}. \tag{18}$$

To start a simulation, we need to determine the density matrix of the system at the initial point of the experiment. We assume that the sample has spent enough time in the prepolarizing magnet to reach thermal equilibrium, that is, the spin system follows Boltzmann's distribution of states. In this case, the density matrix is given by

$$\hat{\rho}_{eq} = \frac{\exp\left(-\frac{\hat{H}}{k_B T}\right)}{Z}, \tag{19}$$

230 where $\hat{H}$, k_B and T are the Hamiltonian operator of the spin system, Boltzmann's constant and the temperature, respectively. Operation $\exp(\quad)$ denotes the matrix exponentiation. Note that this operation does *not* consists of applying $f(x) = \exp(x)$ to each element of the matrix. It is a more complex operation, which is realized in MATLAB by the built-in function *expm* (rather than *exp*). Z is a normalization constant, which ensures that the density matrix has unit trace. It is given by

$$Z = \text{Tr}\left\{\exp\left(-\frac{\hat{H}}{k_B T}\right)\right\}. \tag{20}$$

235 The prepolarizing step of the experiments that we intend to simulate occurs in a strong magnetic field (in the sense that the Zeeman interaction is largely dominating all other interactions). In this case, we can compute the thermal equilibrium taking only the Zeeman terms into account. For a single spin with Larmor frequency ω^0 and gyromagnetic ratio γ in prepolarizing field B_p, the thermal equilibrium density matrix yields

$$\hat{\rho}_{eq} = \frac{\exp\left(-\frac{\hbar\omega^0 \hat{I}_z}{k_B T}\right)}{Z} = \frac{\exp\left(+\frac{\hbar\gamma B_p \hat{I}_z}{k_B T}\right)}{Z} = \begin{pmatrix} \frac{1+P}{2} & 0 \\ 0 & \frac{1-P}{2} \end{pmatrix} = \frac{1}{2}\hat{1} + P\hat{I}_z, \tag{21}$$

where P is the polarization of the nucleus along the z-axis (for positive γ it corresponds to the population excess of the α-state with respect to β-state), defined by

$$P = \tanh\left(\frac{\hbar\gamma B_p}{2k_B T}\right). \tag{22}$$

Note that the use of $\hbar$ in the expression of the Hamiltonian (i.e., expressing the energy in Joules) cannot be avoided here, to ensure consistency of units. To obtain the expression on the right-hand side of (21), we have jumped several steps of calculation which are all based on the definition of polarization. This expression for the density matrix is exact for a spin whose only interaction is the Zeeman interaction, which we have assumed here.

For a n-spin system, we take the Kronecker product of density matrices of individual spins $\hat{\rho}_{eq,l}$

$$\hat{\rho}_{eq} = \otimes_{l=1}^n \hat{\rho}_{eq,l} \approx \otimes_{l=1}^n \left(\frac{\hat{1}}{2} + P_l \hat{I}_z\right), \tag{23}$$

where $\hat{1}$ and $\hat{I}_z$ act on a single-spin Hilbert space (2x2 matrix). The right-hand side expression is approximate in the sense that it neglects all spin-spin interactions.

In many text books(Hore et al., 2015; Levitt, 2013), one encounters simplified expressions of the density matrix. First, it is common to remove the identity component

$$\hat{\rho}_{eq} \rightarrow \hat{\rho}_{eq} - \frac{\hat{1}}{2^n}, \tag{24}$$

where n is the number of spins in the system. Because all operators commute with the identity, this does not affect the result of propagation. The resulting expression is simpler ($\hat{\rho}_{eq} = P\hat{I}_z$ for a single spin) which is convenient for calculations by hand. It may also make the numerical propagation faster and more precise. Another common simplification is to drop the polarization factor. For a single spin, the two combined simplifications yield

$$\hat{\rho}_{eq} \rightarrow \hat{I}_z . \tag{25}$$

Simplifications are useful, but they should be handled with care. The polarization factor P is different for spins with different gyromagnetic ratio. If it is dropped without introducing further corrections, the relative sizes of the population of spins with different gyromagnetic ratio will not be respected. In the simulations presented here, we will compute the initial density matrix using the transformation of (24) but not that of (25).

2.5 Propagate the density matrix under the Hamiltonians

We have seen how to compute the initial density matrix and the matrix representation of the Hamiltonian. We now describe
265 how the evolution of the system (represented by the density matrix) evolves along time under a given Hamiltonian. This will
be used at several steps of the simulation; when the sample is brought adiabatically to ZF, during the pulse and during the
signal measurement.

The evolution of a quantum system along time is given by the time-dependent Schrödinger equation. Its equivalent for the
evolution of density matrix is the Liouville-von Neumann equation. Its solution is sometimes referred to as the "sandwich
270 formula"

$$\hat{\rho}(t) = \hat{U}(t)\hat{\rho}_0\hat{U}^{-1}(t), \tag{26}$$

where $\hat{\rho}_0$ is the density matrix at $t = 0$ and $\hat{U}$ is the propagation operator (or propagator) during time t given defined as

$$\hat{U}(t) = \exp(-i\hat{H}t), \tag{27}$$

where $\hat{H}$ is the total Hamiltonian. The operation of (26) "takes" the spin system from $\hat{\rho}_0$ to $\hat{\rho}(t)$. Again, note that exp( )
275 denotes the matrix exponentiation and *not* element-by-element exponentiation. It is important to remark that (27) is only
valid if the Hamiltonian is constant during the evolution period. The case where the Hamiltonian is time-dependent is treated
below. Note that the propagator is a unitary operator and therefore has the convenient property that its inverse is equal to its
complex conjugate: $\hat{U}^{-1} = \hat{U}^\dagger$, which is much faster to compute than the matrix inverse $\hat{U}^{-1}$.

(26) and (27) allow to know the state of the system at any time t from the initial time $t = 0$. To simulate the signal produced
280 by spin system during the course of the experiment, we must calculate the time domain signal at different time points. Note
that in this case the Hamiltonian remains constant during free evolution. To calculate signal at fixed time steps it is
convenient to first calculate the propagator $\hat{U}(dt)$ over period dt. We then apply (26) recursively to get the new density
matrix $\hat{\rho}(t_{k+1})$ from the previous one $\hat{\rho}(t_k)$

$$\hat{\rho}(t_{k+1}) = \hat{U}(dt)\hat{\rho}(t_k)\hat{U}^{-1}(dt), \tag{28}$$

285 where $t_{k+1} - t_k = dt$. To simulate ZULF spectra, we will also encounter situations where the Hamiltonian is time
dependent. First, the Hamiltonian can vary with time but be "constant by block". This is for example the case for the sudden
field drop; the system is under a certain Zeeman Hamiltonian in the beginning of the experiment and suddenly under the
ZULF Hamiltonian during detection. This situation does not present particular difficulties; the evolution of the system can be
described step by step both by (26) and (28).

290 Second, the Hamiltonian can vary continuously, as in the case of the adiabatic field drop, where the intensity of the magnetic
field is ramped down to zero. Such situation can be simulated by propagating the evolution of the system during time
intervals which are sufficiently short for the Hamiltonian to be considered constant during this time interval. The propagator
must then be computed for each time increment. The form of the equation for propagation is similar to (28)

$$\hat{\rho}(t_{k+1}) = \hat{U}(t_k \rightarrow t_{k+1})\hat{\rho}(t_k)\hat{U}^{-1}(t_k \rightarrow t_{k+1}), \tag{29}$$

295 where the propagator is given by

$$\hat{U}(t_k \rightarrow t_{k+1}) = \exp(-i\hat{H}(t_k)dt), \tag{30}$$

where $\hat{H}(t_k)$ is the Hamiltonian at time t_k. Note that the choice of $\hat{H}(t_k)$ rather than $\hat{H}(t_{k+1})$ in (30) is arbitrary but in the limit of small intervals, the choice has no consequence.

2.6 Extract expectation values from the propagation

300 The propagation procedure described above gives access to the density matrix along time. To simulate the time domain signal, we need to extract a physical quantity from the density matrix as it evolves with time. The measured physical quantity of a ZULF experiment is the magnetic field produced by the nuclear spins of the sample at the location of an OPM. In first approximation, we can consider the whole sample as a point dipole interacting with the OPM and that this total dipole is the sum of the dipole of the individual spin systems (Figure 2 gives a visual representation of the approximation). Whether this

305 approximation is appropriate or not depends on the geometry of the experimental setup. We have chosen the *z*-axis as the quantization axis (defined by the detector, i.e., the OPM). Therefore, the physical quantity that we need to compute is the total magnetic field produced by the spins along the *z*-axis at the location of the vapor cell

$$\langle B_z \rangle = \frac{\mu_0}{2\pi} \frac{\langle \hat{\mu}_z^{tot} \rangle}{r^3} = \frac{\mu_0}{2\pi} \frac{N\langle \hat{\mu}_z \rangle}{r^3}, \tag{31}$$

where $\langle \hat{\mu}_z^{tot} \rangle$, μ_0, N, $\langle \hat{\mu}_z \rangle$ and r are the magnetic moment of the sample along the *z*-axis, the permeability of free space, the

310 number of identical spin systems in the sample, their individual magnetic moment along the *z*-axis and the distance between the center of the sample and the center of the vapor cell, respectively.
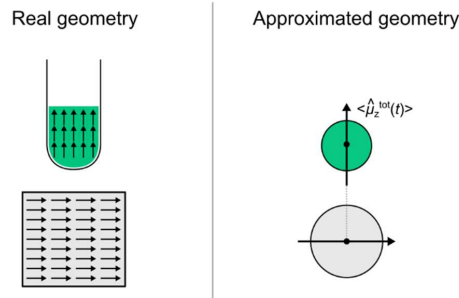
Figure 2: Comparison of the real geometry of the sample of the OPM with the approximated one. The arrows represent local magnetization vectors parallel to the total magnetization vector.

For each identical spin system, we then compute the magnetic moment as the sum of the contributions of each spin l.

$$\langle B_z \rangle = \frac{\mu_0}{2\pi} \frac{N}{r^3} \sum_{l=1}^{n} \langle \hat{\mu}_{z,l} \rangle = \frac{\mu_0}{2\pi} \frac{N\hbar}{r^3} \sum_{l=1}^{n} \gamma_l \langle \hat{I}_{z,l} \rangle, \tag{32}$$

where $\mu_{z,l}$, γ_l and $I_{z,l}$ are the magnetic moment, the gyromagnetic ratio and the angular momentum along the z-axis of spin l,

315   respectively. The notation $\langle \ \rangle$ denotes the expectation value of a quantity. Particularly important ones are those that can be physically measured in the experiment. In the density matrix formalism that we are using, the expectation value of a physical quantity related to an operator $\hat{A}$ is given by

$$\langle A \rangle = \text{Tr}\{\hat{A}\hat{\rho}\}, \tag{33}$$

320   where $\text{Tr}\{\ \}$ denotes the matrix trace, *i.e.* the sum of all diagonal elements of the matrix representation of the operator. Note that the expectation value of $\hat{\mu}_{z,l}$ (or $\hat{I}_{z,l}$) is proportional to the polarization level of spin l which was accounted for in (21) and (22). Therefore, the total magnetic moment calculated with (32) depends on the polarization of the different spin species. If $\hat{\rho}(t)$ is the density matrix at time t, we obtain the signal $S(t)$ measured by the OPM by plugging (32) into (33)

$$S(t) = \langle B_z \rangle(t) = \frac{\mu_0}{2\pi} \frac{N\hbar}{r^3} \text{Tr}\{\hat{O}\hat{\rho}(t)\}, \tag{34}$$

325   where we have defined a "detection operator"

$$\hat{O} = \sum_{l=1}^{n} \gamma_l \hat{I}_{z,l}. \tag{35}$$

To obtain (34), we have used the fact that taking the trace of a matrix is a linear operation and so the trace of a sum is the sum of the traces.

In the case of a sample with volume $V = 100$ μL of ^{13}C-formic acid prepolarized at 2 T at 298 K, with molar mass of 46

330   g/mol and density of 1.22 g/ml one finds that the amplitude of oscillating magnetic field generated by the sample at distance of $r = 1$ cm is of the order of 10 pT using the above equations. This estimation does not take into account demagnetization effects caused by distribution of spins in space, giving the upper limit for the expected field. Experimentally measured magnetic fields are about 10 times smaller (Tayler et al., 2017).

2.7 Fourier transform the expectation values to obtain a spectrum

335   The time domain signal is what is measured by the ZULF NMR spectrometer. The final step of the simulation is to transform the measured signal from the time domain to the frequency domain using a discrete Fourier transform. Programming environments such as MATLAB or *Mathematica* are equipped with built-in fast Fourier transform functions. We will not discuss the mathematics behind this process but we will give a few practical hints. Contrary to high-field NMR, ZULF spectra can be obtained with real magnetic field units (rather than arbitrary units). We will show how such units can be

340   obtained.

Let us call $\vec{t}$ and $\vec{S}$ the vectors containing the time and corresponding time domain signal values, respectively, which resulted from the previous steps. We call these objects vectors in reference to the way they are constructed in MATLAB's environment. Let us call K the number of elements of both vectors (which corresponds to the number of points in the time domain signal). For now, $\vec{S}$ consists of a sum of oscillating signals which do not decay with time because our simulation did not include relaxation effects. If we perform a Fourier transform on $\vec{S}$, we will obtain non-Lorentzian lineshapes (with distinctive sinc patterns). We must therefore artificially include relaxation by multiplying the signal with an apodization function, to force the signal to decay to 0. For liquid state signals, the most common choice is a monoexponential decay which can be expressed as:

$$S'_k = S_k \exp(-\pi l_B t_k) = S_k \exp\left(-\frac{t_k}{T_2}\right), \tag{36}$$

where S_k, t_k, l_B, T_2 are the kth elements of $\vec{t}$ and $\vec{S}$, the line broadening in Hz and the coherence time constant in s, respectively. S'_k defines the apodized signal vector $\vec{S'}$. As show in (36), we may choose to express the apodization function either using the coherence time constant T_2 or the line broadening l_B, which are related by $\pi l_B = 1/T_2$ The former is the time constant at which the time domain signal decays while the latter is the full width at half height (FWHH) of the signals on the Fourier transform. In order to avoid "truncating" the decay of the time domain signal and the related spectral artefacts, we must fulfil the condition $T_2 \ll t_{aq}$, where $t_{aq} = \max\{t_k\}$ is the acquisition time (or the length of the signal in the time domain). Typically, we may choose T_2 and t_{aq} so that $t_{aq} = 5T_2$. Table 1 summarizes the parameters which were used in this Paper.

The apodization function of (36) yields Lorentzian signals as one would expect. However, without further apodization, the baseline of the spectra will have some distortions (Zhu et al., 1993), with the main distortion being a small offset of the baseline. This problem arises because the time domain signal has its first point at time $t = 0$, so that the Fourier transform gives the integral of the first segment of twice larger amplitude than it should be. As proposed by Otting, this baseline offset can be removed by weighting the first point of the time domain signal by factor ½ (Otting et al., 1986). However, because the integral of the Fourier transform is proportional to the first point of the time domain signal, this apodization does not preserve the integral. To obtain spectra without baseline offset and preserving the integral, we propose to use an apodization function which weights all points by 2 expect for the first one

$$S''_k = \begin{cases} S'_k & \text{if } k = 1 \\ 2S'_k & \text{otherwise} \end{cases}. \tag{37}$$

In MATLAB programming language, the fast Fourier transform function *fft()* takes vector $\vec{S'}$ as input and returns the frequency domain vector which corresponds to the simulated spectrum. Optionally, one may add a second argument L to *fft()* to include zero-filling in the Fourier transform. Including zero filling has the advantage of increasing the number of points per FWHH on the spectrum without increasing the computation time of the propagation. Due to MATLAB's Fourier

transform convention, it is convenient to retransform the signal with *fftshift()* in order to obtain a Fourier transformed signal with 0 as the middle frequency. We then divide the the output of the MATLAB's Fourier transform by the number of points L

$$S(\nu) = \frac{1}{L} \mathcal{F} \, S(t),\tag{38}$$

375 where $\mathcal{F}$ designated the Fourier transform. The frequency domain signal obtained after this whole procedure has units of magnetic field (e.g. pT). Changing the zero-filling L changes the intensity of the frequency domain signal but preserves the integrals.

MATLAB's *fft()* functions do not generate the frequency vector associated with the Fourier transformed signal. The frequency vector $\vec{\nu}$ in Hz can be generated based on the following expression

380 $$\nu_k = \frac{k}{L} f, \ k \in \left[\!\left[-\frac{L}{2} ; \frac{L}{2} - 1 \right]\!\right],\tag{39}$$

where the sampling frequency in Hz is given by

$$f = \frac{K-1}{t_{aq}}.\tag{40}$$

The sampling frequency of the time domain signal gives the maximum frequency that can be appropriately sampled. Figure 3 illustrates the consequence of choosing a sampling frequency which is lower than the maximum frequency. If the sampling
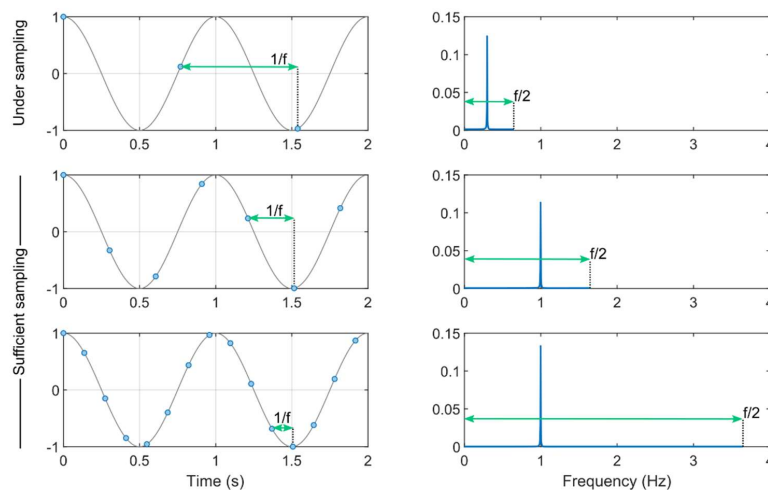
Figure 3: Illustration of signal sampling and the effect of undersampling. The left panels represent a cosine oscillating at 1 Hz in grey sampled with various frequency f (1.3, 3.7 and 7.3 Hz). The blue dots represent the samples. In each case, the Fourier transform is shown on the right panels. When the sampling frequency is lower than 1 Hz, the peak cannot appear at 1 Hz and is therefore found at a fictitious position.

385 frequency is lower than the signal to be sampled, the Fourier transformed signal lies outside the spectral width (between $-f/2$ and $+f/2$). However, due to the "refolding effect" of the Fourier transform, the signal still appears on the spectrum but at irrelevant positions. To avoid this, one may repeat the simulation increasing the sampling frequency and keeping other parameters constant. If the sampling frequency is sufficient, the spectrum should not be affected.

The choice of the parameters discussed in this section and above influences the outcome of the simulation in the same way

390 as it does for the experiment. Once an NMR simulation is running, one might want to play with combination of f, K, t_{aq}, T_2 and L until the simulated spectra display convenient features. If one intends to simulate spectra to match experimental data, one might simply perform the simulation with the same f, K, L, and t_{aq} values. Table 1 summarizes the parameters which were used in this Paper.

Parameter name	Meaning	Value used in Figure 4
K	Number of points of the time domain signal	4096
L	Number of points of the time domain signal including zero filling / number of points of the Fourier transform	65536
t_{aq}	Acquisition time	5 s
f	Sampling frequency or spectral width	819.200 Hz
τ_d	Dwell time (time between acquisition points)	1.2207 ms
T_2	Coherence's relaxation time constant	1 s
l_b	Line broadening	0.3183 Hz

Table 1: List of parameters that were used to simulate the time domain signals and spectra in Figure 4.

395

The procedure described here yields an NMR signal which is symmetric around 0. As a consequence, each signal is found both in the positive and negative frequencies and the integral is split into the two duplicates. Because the experimental procedure that we are simulating does not differentiate negative and positive frequencies, we discard the frequency domain signal corresponding to negative frequencies and multiply the frequency domain signal corresponding to positive frequencies

400 by a factor 2. This operation corresponds to "folding" the spectrum around $\nu = 0$. Note that in high-field NMR, the measured signal is complex and is therefore not split into a positive and a negative half.

Whether the time domain signal which results from the simulation is real or complex, the Fourier transform yields a complex frequency domain signal. To get a spectrum consisting of a signal intensity as a function of the frequency, we must use the real part the frequency domain signal. Depending on the experiment that we are simulating, we might find that some or all

405 spectral components of the frequency domain signal are not in phased. To compensate for this, one might apply a phase

correction by multiplying each point of the frequency domain signal by a complex constant $\exp i\phi$ where ϕ is the phase correction before taking its real part

$$I_r(\nu) = \mathrm{Re}\{I_c(\nu)\exp i\phi\}, \tag{41}$$

where $I_r(\nu)$ and $I_c(\nu)$ are the real and complex frequency domain signals, respectively.

410 In summary, the Fourier transform procedure that we have described has the following steps:

1. Apply a monoexponential apodization window to the time domain signal so that it decays to 0 (see (35))
2. Apply the apodization described by (36) to avoid baseline artefacts on the frequency domain signal
3. Obtain the complex frequency domain signal by Fourier transforming the time domain signal using a fast Fourier transform algorithm
415 4. Generate the corresponding frequency axis using (39) and (40)
5. Remove the negative frequencies from both the frequency axis and the frequency domain signal and multiply the frequency domain signal by 2 to account for the partition of the signal integral between positive and negative frequencies
6. Take the real part of the signal

420 **2.8 Comparison with high-field NMR**

We conclude this theory section by listing the main differences between high-field and ZULF NMR, which are summarized in Table 2. As is the case for the rest of the paper, our description is limited to small molecules containing spin-1/2 in the liquid state.

At high magnetic field, the Zeeman interaction dominates the dynamics and the *J*-coupling and the chemical shift only 425 represent small perturbations. At ZULF, the *J*-coupling dominates while the Zeeman interaction is a perturbation and the chemical shift plays no role. In Figure 1 and in the simulations presented in this paper, we have assumed that the detector was position below the sample (along the *z*-axis in our axis convention) and that it was sensitive to magnetic field along the *z*-axis. Although this choice is typical, it is not the only possibility. In common high-field experiments, the oscillating signal emitted by the spins is recorded perpendicular to the static magnetic field. Detection at ZULF is performed with 430 magnetometers, which are sensitive to the total magnetic field produced by the sample. The operators corresponding to this observable is the sum of the magnetic moment of the spins along the quantization axis. In typical experiments, a single detector is used, which results in real signal. Note that using several detectors placed adequately, an imaginary ZULF signal could be obtained. High-field NMR uses Faraday induction in pick-up coils. Signals originating from different nuclei are usually not observed in the same experiment because their Larmor frequencies are too far apart and the NMR coils are 435 sensitive over a limited bandwidth. The operators corresponding to inductive detection in pulsed NMR is non-Hermitian and therefore yields complex signals.

	ZULF	**High-field**
Main interaction	J-coupling $\hat{H}_J$	Zeeman interaction $\hat{H}_Z$
Perturbations	Zeeman interaction $\hat{H}_Z$	J-coupling $\hat{H}_J$, chemical shift $\hat{H}_{CS}$
Detection method	Magnetometry (OPM, SQUID, NV, …)	Faraday induction
Observables	$\hat{\mu}_{S,z} + \hat{\mu}_{I,z} = \gamma_I \hat{I}_z + \gamma_S \hat{S}_z$	$\hat{I}_- = \hat{I}_x - i\hat{I}_y$
Signal type	Real	Complex

Table 2: Comparison between high-field and ZULF NMR for typical experiments. Note that quadrature detection (and thus imaginary signals) is possible at ZULF, although uncommon.

3 Results of numerical simulations

3.1 Excitation schemes on an XA spin system

The ZF and ULF spectra of an XA spin system with a J-coupling of 140 Hz were simulated for different experimental sequences, assuming that the sample consists of 100 µL of solution where the spin system has a concentration of 27 mol.L⁻¹. Figure 4 shows the experimental sequences, the simulated time domain and frequency domain signals. For all simulations, the sample was assumed to have spent sufficient time in a prepolarizing field of 2 T at 298 K to be at Boltzmann's equilibrium. The polarizations of the ¹³C and ¹H spins were calculated using Boltzmann's distribution (see (19)) and used to compute the single-spin density matrices of the ¹³C and ¹H spins, $\hat{\rho}_{eq}(^{13}C)$ and $\hat{\rho}_{eq}(^1H)$ (see (21)). The density matrix of the two-spin system was computed taking the Kronecker product of the single-spin density matrices $\hat{\rho}_0 = \hat{\rho}_{eq}(^{13}C) \otimes \hat{\rho}_{eq}(^1H)$ (see (23)). The identity was removed from the 2-spin density matrix using (24). The resulting density matrix was assumed to represent the initial state of the simulation (as explained above, only the Zeeman terms are considered to contribute to the initial state). For each experimental sequence, the spectrum was simulated both at 0 nT (including only the J-Hamiltonian $\hat{H}_J$, see (12)) and with a field of 0.5 µT along the x-axis, that is, orthogonal to both the direction of the prepolarizing field and the sensitive axis (including both the J-Hamiltonian $\hat{H}_J$ and the Zeeman Hamiltonian $\hat{H}_Z$, see (12) and (10)). The time domain signal was computed by propagating the density matrix under the effect of the Hamiltonian for a total time of 5 s (parameter t_{aq}) discretized into 4096 points (parameter K), corresponding to time intervals dt of 1.2207 ms (parameter τ_D). Prior to the propagation loop, the ZF and ULF propagators for this particular time step $\hat{U}$ (see (30)) and the observable operator $\hat{O}$ (see (40)) were computed only once.

The density matrix was propagated from time t_k to time $t_{k+1} = t_k + dt$ under the Hamiltonian (ZF or ULF) using the sandwich formula $\hat{\rho}_{k+1} = \hat{U}\hat{\rho}_k\hat{U}^{-1} = \hat{U}\hat{\rho}_k\hat{U}^\dagger$ (see (29)). At each time point k of the propagation (realized by a for loop), the

signal intensity of the time domain signal was extracted from the density matrix using the trace $\text{Tr}\{\hat{O}\hat{\rho}_k\}$ (see (33)) in pT. In theory, the trace of Hermitian operator should be real. However, due to the finite machine precision of the numeric algorithm, the trace can sometimes contain a non-zero imaginary part. This residual imaginary part is discarded by taking the real part of the trace $\text{Re}(\text{Tr}\{\hat{O}\hat{\rho}_k\})$. This point might appear secondary but dealing with complex numbers while thinking they are real can lead to important mistakes. After propagation, a monoexponential apodization function was applied to the time-domain signal (see (36)), with a coherence time constant T_2 of 1 s. A second apodization functions was applied to avoid baseline artifacts (see (39)). The apodized time domain signal was Fourier transformed with zero-filling to 65'536 points, using MATLAB's built-in functions. The real part of the Fourier transform is shown on Figure 4. The frequency axis of the spectra was computed using (39) and (40). The spectra are symmetric around zero and so it is common to work only with the positive frequencies as shown in Figure 4.

Simulating the sudden field drop experiment is the simplest case presented here. Because the coherence excitation scheme (or mixing) only consists of bringing the spin from high magnetic field to ZF or ULF, the simulation only consists of propagating the high-field thermal equilibrium density matrix under the ZF or ULF Hamiltonian. The ZF spectrum consists of one line at the J-coupling and one at zero frequency (see Figure 4A). Including a field of 0.5 μT field along the x-axis (ULF case) splits the J-peak as well as the line at zero frequency.

The simulations presented in Fig. 4B-D feature an adiabatic field drop. We used a monoexponential field drop from $B_{start} = 200$ μT to 0 occurring over $t_{decay} = 0.5$ s with a decay time constant of $\tau = 0.05$ s, described by

$$B(t) = B_{start}\frac{\exp\left(-\frac{t}{\tau}\right)-\exp\left(-\frac{t_{decay}}{\tau}\right)}{1-\exp\left(-\frac{t_{decay}}{\tau}\right)}, \tag{42}$$

which fulfils the conditions $B(0) = B_{start}$ and $B(t_{decay}) = 0$.

During the field drop, the Hamiltonian $\hat{H}(t) = \hat{H}_J + \hat{H}_Z(t)$ is time-dependent. This step thus cannot be simulated in a single propagation step. Instead, it must be discretized in sub-steps dt that are sufficiently short for the Hamiltonian to be considered time-independent. Here, the 0.5 s time length was discretized into 5000 steps of 0.1 ms. At time $t = 0$, the density matrix is the thermal equilibrium density matrix $\hat{\rho}_{eq}$ obtained above. At each time step t_k, the propagator $\hat{U}(t_k \rightarrow t_{k+1}) = \exp(-i\hat{H}(t_k)dt)$ is computed (see (30)) and the density matrix is propagated from time t_k to time $t_{k+1} = t_k + dt$ (see (29)) under the Hamiltonian $\hat{H}(t_k) = \hat{H}_J + \hat{H}_Z(t_k)$. We name $\hat{\rho}_{adia}$ the density matrix obtained after this process. A question arises here: is this magnetic field drop that we have chosen sufficiently slow to be considered adiabatic? In other words, is $\hat{\rho}_{adia}$ stationary? A simple way to ensure that it is the case is to simulate the spectrum at ZF after the magnetic field drop without any excitation pulse, that is, taking $\hat{\rho}_{adia}$ as the density matrix at time $t = 0$, $\hat{\rho}_0$. If the transition is adiabatic, the system should remain stationary i. e. the time-domain signal should feature no oscillation and the spectrum no peak. Figure 4B shows the result of this procedure, which confirms that the transition is adiabatic. The only feature of the ZF spectrum in Figure 4B is the line at zero-frequency. This line originates from the non-oscillating magnetization decaying

490 with T_2 which is the result of the apodization function that we have applied. Verifying that the spectrum ZF spectrum is flat also ensures that the field drop was discretized in sufficiently short time intervals dt.
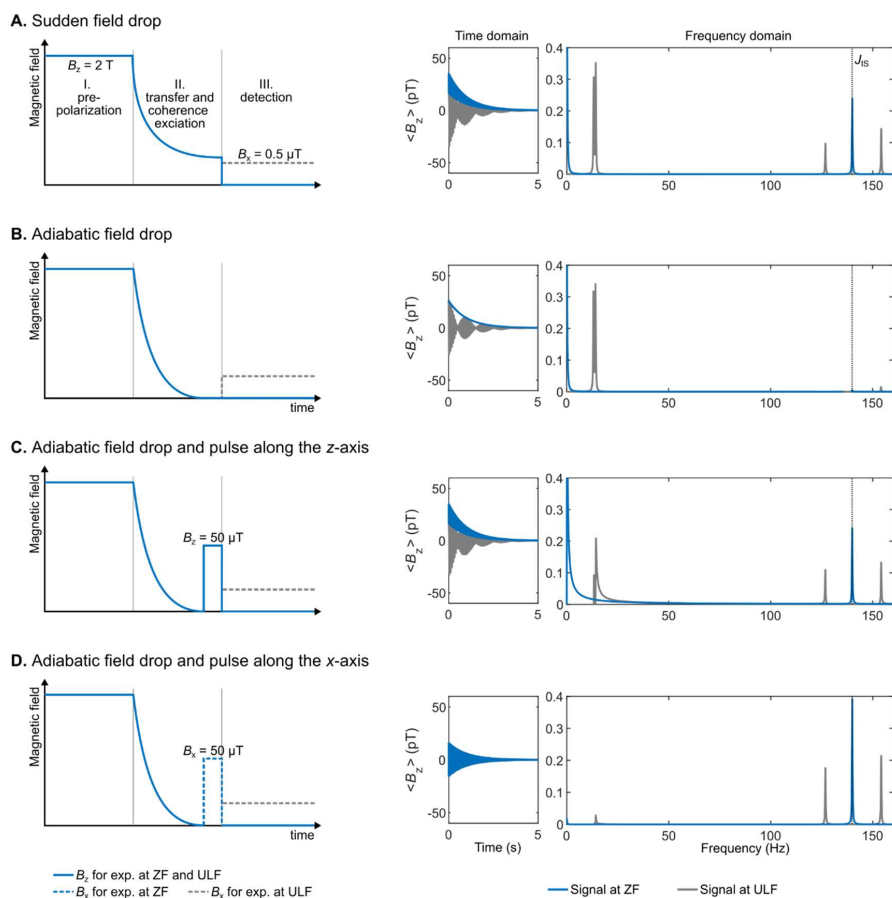
Figure 4: Excitation schemes for an XA spin system corresponding to a ^{13}C and ^{1}H spins with a *J*-coupling of 140 Hz and corresponding simulated time domain signals and spectra. The vertical dashed line indicates the J-coupling. The time domain signal was computed by propagating the density matrix under the effect of the Hamiltonian for a total time of 5 s (parameter t_{aq}) discretized in 4096 points (parameter *K*), corresponding to time intervals dt of 1.2207 ms (parameter τ_D). A monoexponential apodization function was applied to the time domain signal, with a coherence time constant T_2 of 1 s. The apodized time domain signal was Fourier transformed with a zero-filling of 65'536 points.

The density matrix after the adiabatic field drop $\hat{\rho}_{adia}$ obtained above was used for the simulations presented in Fig. 4C-D. In the experimental sequences of Fig. 4C-D, the adiabatic field drop is followed by a magnetic field pulse either along the *z*- or *x*-axis. This was simulated by propagating $\hat{\rho}_{adia}$ under the pulse Hamiltonian to obtain $\hat{\rho}_0 = \hat{U}_p(\tau_p)\hat{\rho}_{adia}\hat{U}_p^\dagger(\tau_p)$, where

495    $\hat{U}_p(\tau_p)$ is the propagator of the pulse Hamiltonian $\hat{H}_p = \hat{H}_J + \hat{H}_Z$, which acts on the density matrix during pulse length τ_p. The Zeeman Hamiltonian depends on the magnetic field intensity of the pulse B_p and its direction (see (4)). For the *z*-axis pulse, we used a pulse intensity and length of 50 µT and 150 µs, respectively. For the *x*-axis pulse, we used a pulse intensity and length of 50 µT and 910 µs, respectively. These choices are justified in the next section. The resulting density matrices $\hat{\rho}_0$ were used as the density matrix at time $t = 0$ of the time-domain signal, which was computed and Fourier transformed as

500   described above. In the case of the *z*-axis pulse experiment, the peaks of interest (*J*-peak at 140 Hz) were found to be out of phase; a phase correction $e^{i\phi}$ with $\phi = \pi/2$ was thus applied to the Fourier transform. Adjusting the phase for the *J*-peak caused the lower-frequency peaks to be out of phase. Interestingly, in Figure 4D, the intensity of the *J*-peak is higher than for the other excitation schemes while the lower-frequency peaks are suppressed, indicating that all the available polarization has been transferred to the *J*-peak.

505   **3.2 Nutation experiments**

The pairs of magnetic field intensity and length of the pulses used for the simulation in Figure 4D were chosen by simulating "nutation curves" both for the *z*- and *x*-axis pulses. In high-field NMR, the nutation experiment consists of recording a series of NMR detections keeping the RF pulse power constant and varying the pulse length (or the pulse length is kept constant and the amplitude is varied(Tayler et al., 2017)). The nutation curve is the plot of the signal intensity as a function of the

510   varied parameter. It allows to determine the pair of RF power and pulse length which maximizes the signal intensity. Except in the presence of rapid relaxation effects or RF field inhomogeneities, the observed nutation curve is sinusoidal. At ZULF, the nutation curve is more complex and depends on the spin system under scrutiny. To simulate the nutation experiment at ZF, we repeated the simulation of the ZF spectra for an experiment with an adiabatic field drop (using the same parameters as above) followed by a pulse of 50 µT along the *z*- and *x*-axis, varying the pulse length from 0 to 3000 µs. The time-domain

515   signal was Fourier transformed as described above and the frequency-domain signal was integrated from 138 to 142 Hz. The signal integral of the *J*-peak is plotted as a function of the pulse length in Figure 5. The signal integral of the sudden drop experiment is shown as a horizontal dashed line for comparison. When a pulse along the *z*-axis is used, a simple sinusoidal curve is obtained and its maximum matches that of the sudden drop experiment (see Figure 5A).

The first maximum is reached for pulse length of 150 µs. When a pulse along *x*-axis is used, a more complex pattern is

520   obtained and the maximum is found to be 1.64 times higher than the sudden drop experiment (see Figure 5B). The first global maximum is reached for pulse length of 910 µs.
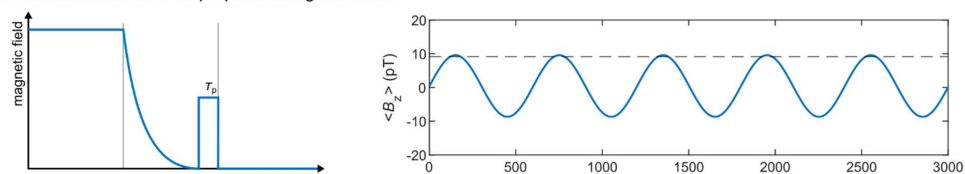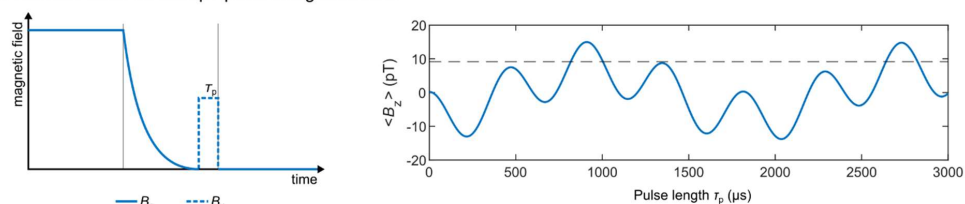
Figure 5: Nutation curves at ZF with excitation pulses along z- and x-axes. The horizontal dashed line represents the signal integral of the sudden drop ZF experiment. The time domain signal was computed by propagating the density matrix under the effect of the Hamiltonian for a total time of 5 s (parameter t_{aq}) discretized in 4096 points (parameter K), corresponding to time intervals dt of 1.2207 ms (parameter τ_D). A monoexponential apodization function was applied to the time domain signal, with a coherence time constant T_2 of 1 s. The apodized time domain signal was Fourier transformed with a zero-filling of 65'536 points. The frequency domain signal was then integrated from 138 to 142 Hz. The nutation curve represents the integral compared with the excitation pulse length. pT should be recalculated.

3.3 XA$_n$ spin system

The simulations shown up to this point only deal with an XA spin system, which typically corresponds to ^{13}C-formate (or ^{13}C-formic acid), where the ^{13}C spin interacts with a single ^{1}H through a J-coupling of 195-222 Hz (Blanchard and Budker, 2016; Tayler et al., 2017) (depending on experimental conditions). ^{13}C,^{15}N-cyanide groups are also interesting two-spin systems which were used in ZULF experiments (Blanchard et al., 2020, 2015). We now extend the simulation to incorporate multiple X spins. An XA$_2$ spin system is for example met in ^{13}C-glycine(Put et al., 2021). XA$_3$ spins are met in a number of molecules containing methyl groups such as ^{13}C-pyruvate (Barskiy et al., 2019). XA$_4$ (for example ^{15}N-ammonium cation(Barskiy et al., 2019)) and XA$_5$ are less common but they are presented here to show the pattern that arises when adding spins.

Figure 6 shows the simulations for sudden drop experiments with detection at ZF and ULF of XA$_n$ spin systems with n = 1, 2, … 5 where X is a ^{13}C spin and A$_n$ are ^{1}H spins with a J-coupling of 140 Hz between X and A spins and 10 Hz among A spins. All the relevant mathematics to construct the operators of a $m = n + 1$ spin system is given in the Theory Section. For an XA$_5$ spin system, the Hilbert space has $2^6 = 64$ dimensions (and related operators). To avoid constructing each operator manually, recursive formulae were used (see (13) and (23)). The time-domain signal was computed by propagating the density matrix under the effect of the Hamiltonian for a total time of 5 s (parameter t_{aq}) discretized into 8192 points
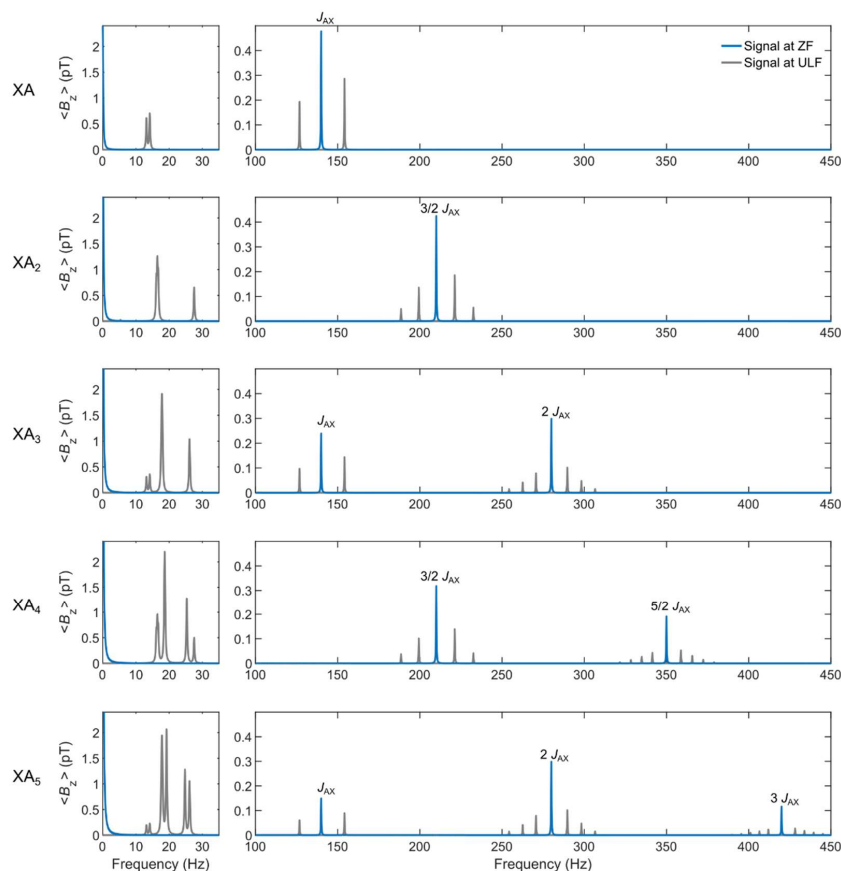
Figure 6: Simulation of ZF and ULF spectra after sudden field drop for XA, XA₂, XA₃, XA₄ and XA₅ spin systems with a J-coupling of 140 Hz between X and A spins and 10 Hz among A spins. The time domain signal was computed by propagating the density matrix under the effect of the Hamiltonian for a total time of 5 s (parameter t_{aq}) discretized into 4096 points (parameter K), corresponding to time intervals dt of 1.2207 ms (parameter τ_D). A monoexponential apodization function was applied to the time domain signal, with a coherence time constant T_2 of 1 s. The apodized time domain signal was Fourier transformed with a zero-filling of 32'768 points.

(parameter K), corresponding to time intervals dt of 0.6104 ms (parameter τ_D). A monoexponential apodization function was applied to the time domain signal, with a coherence time constant T_2 of 1 s. The apodized time domain signal was Fourier transformed with a zero-filling of 32'768 points.

540   Increasing the number of A spins increases the number of spectral components in the spectrum. A known result of ZULF NMR appears on this simulation: for odd numbers of n, the ZF spectrum features lines at integer multiples of the J-coupling

$k*J_{AX}$ with $k \in [\![1; (n+1)/2]\!]$ while for even number of n, it features lines at half-integer multiples of the J-coupling coupling $k*J_{AX}/2$ with $k \in [\![1; n/2]\!]$. Adding a 0.5 µT field along the x-axis during detection (that is, performing ULF detection) splits the J-lines. The higher the frequency, the greater the number of splittings. Note that the intensity of NMR

545   signals at high-field increase upon adding more equivalent spins to the spin system. The analysis of Fig. 6 shows that this logic does not apply to the J-lines for the ZULF case, where the spectrum completely changes upon changing of spin topology. For example, note that the amplitude of the J-line for the XA system has the same intensity as the J-line for the XA_2 system (appearing at $3/2*J_{AX}$ frequency). Likewise, the two J-lines for the XA_3 system has the same total intensity as the two J-lines for the XA_4 system. An empirical law of conservation of the total spectral intensity for the J-lines can be

550   deduced by looking at Fig. 6: indeed, the total intensity of all J-lines is the same for any XA_n system, assuming equal sample volume, prepolarization, *etc*. On the other hand, the intensity of low frequency peaks shown in Fig. 6 is proportional to the total number of spins in the spin system, like in high-field NMR. This is of course expected as these signals are associated with the precession of total magnetization around residual ULF field, and total magnetization is proportional to the number of spins.

555   **4 Interpretation**

We are now going to show how to calculate ZULF NMR spectra considering energy levels and transition probabilities rather than through the numerical propagation of the density matrix. We will derive analytical solutions for the XA_n system in particular but the same approach can be used for more complex spin systems. This approach was investigated in references (Butler et al., 2013a; Theis et al., 2013; Emondts et al., 2014). Here we aim to present it with more explanations and explicit

560   derivations but we limit ourselves to only the simplest spin systems.

The relative contribution of $\widehat{H}_z$ (see (10)) and $\widehat{H}_J$ (see (12)) terms depends on the magnetic field strength. In the high-field extreme, for a heteronuclear spin system, $\widehat{H}_z$ is the dominant term and $\widehat{H}_J$ is considered as a first-order perturbation. In this case, heteronuclei are said to be weakly coupled and their eigenstates coincide with the Zeeman states (e. g. those in (9)). At zero-field, the weak coupling approximation is not valid, the Zeeman states do not correspond to the eigenstates of system.

565   However, it is still possible to calculate analytically the eigenstates for some spin systems, and the simplest case is when all the spins are identical (A_n system). In this case, the Hamiltonian is represented by only the $\widehat{H}_J$ term and it commutes with the square of the total angular momentum operator

$$\widehat{F}^2 = \widehat{F}_x^2 + \widehat{F}_y^2 + \widehat{F}_z^2$$

$$\widehat{F}_k = \sum_{a=1}^n \widehat{I}_{a,k}; \; k \in \{x, y, z\}, \tag{43}$$

570    $$[\widehat{H}_J, \widehat{F}^2] = \widehat{H}_J \widehat{F}^2 - \widehat{F}^2 \widehat{H}_J = 0$$

where n is the number of spins in the system. It is well known that any pair of commuting Hermitian operators share their eigenspaces.(Levitt, 2013) The set of eigenstates which forms an eigenbasis for both operators simultaneously is unique in cases where there are no degeneracies (all the eigenvalues for both operators are different). When there are degeneracies, the common eignenbasis is not unique. It turns out that $\hat{H}_J$ and $\hat{F}^2$ operators have degeneracies, and this results in the existence
575   of an infinite number of different shared eigenbases. Let us describe how to find such a set of eigenstates.

4.1 Eigenstates at zero-field

The eigenstates of a $\hat{F}^2$ operator can be expressed in terms of the total spin and its projection quantum numbers. The conventional way for expressing them is to use the $|F, m_F\rangle$ notation, where F denotes the total spin and m_F denotes the projection onto a quantization axis ($m_F \in \{-F, -F + 1, \dots, F - 1, F\}$). For example, by definition, for a single spin 1/2, we
580   have the sates $|\alpha\rangle \equiv \left|{}^1/_2, {}^1/_2\right\rangle$; $|\beta\rangle \equiv \left|{}^1/_2, -{}^1/_2\right\rangle$. For a pair of spins, we have the three triplet states: $|T_{+1}\rangle \equiv |1,1\rangle$; $|T_0\rangle \equiv |1,0\rangle$; $|T_{-1}\rangle \equiv |1,-1\rangle$, and the singlet state $|S_0\rangle \equiv |0,0\rangle$. Any $|F, m_F\rangle$ state is an eigenstate of the $\hat{F}^2$ and $\hat{F}_z$ operators with the following eigenvalues

$$\begin{aligned}\hat{F}^2|F, m_F\rangle &= F(F + 1)|F, m_F\rangle \\ \hat{F}_z|F, m_F\rangle &= m_F|F, m_F\rangle\end{aligned}. \tag{44}$$

To find the total spin of a system constituted by n spins, one must sum up the angular momenta of the individual spins,
585   which is a common procedure in the field of atomic physics but not so much in NMR. All possible values of the angular momentum of the interacting spins are added up to constitute a set of uncoupled quasiparticles with different total spin. The total spin F of a system constituted by two spins I and S can take the values with steps of 1 between the sum $I + S$ and the absolute value of their difference

$$|I - S| \le F \le I + S. \tag{45}$$

590   For a pair of spins 1/2, the possible values are $F = 0,1$. For n spins, the summation should be proceeded until all the possible pairs of the angular momentum of the individual spins are summed up. As an illustration, consider a coupled system of 3 spins ½ (see Figure 7). First, any two spins are added up together to give $F = 1$ (a triplet) and $F = 0$ (a singlet). Then, the remaining spin-1/2 is added up to the quasiparticles formed in the previous step (spins 1 and 0 in this case). As a result, the initial A₃ system is decomposed into three subsystems with total spins of $F = 3/2$, 1/2, (addition of 1 and 1/2) and $F =1/2$
595   (addition of 0 and 1/2).
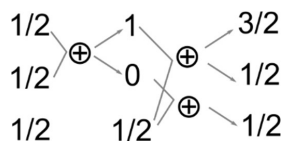
Figure 7: Procedure for adding up the angular momenta for the A₃ spin system

A useful property of such decomposition can be illustrated at this point: the total spin commutes with all rotation operators
600 (e.g. $\exp(-i\theta\hat{I}_z)$) and therefore 3D rotations will never mix terms of the wavefunction belonging to different total spin, e.g. spin 3/2 with 1/2. At ZF there is no distinction between directions and therefore the eigenstates must be invariant with respect to 3D rotations. This also partially explains the existence of infinite number of eigenbases for $\hat{F}^2$, as all different orientations of $\{x, y, z\}$ system correspond to different bases.

One can check that the total number of the spin states remains the same after the procedure of adding up the spins. On the
605 one hand, the number of states formed by n coupled spins I equals to $(2I + 1)^n$, which is 8 in the considered case. On the other hand, a manifold with a total spin F has $2F + 1$ different states associated with different possible projections of the spin on the quantization axis. Therefore, there are $4 + 2 + 2$ states in the considered case.

The explicit form of the resulting eigenstates can be obtained in terms of "uncoupled" spin states, which are constructed as Kronecker product of the individual Zeeman states (see (9)). The resulting state $|F, m_F\rangle$ of the addition of two angular
610 momenta (I and S) can be represented as the following linear combination

$$|F, m_F\rangle = \sum_{m_I, m_S} C^{F, m_F}_{I, m_I, S, m_S} |I, m_I, S, m_S\rangle, \tag{46}$$

where $C^{F, m_F}_{I, m_I, J, m_J}$ are called Clebsch-Gordan coefficients and are defined by

$$C^{F, m_F}_{I, m_I, S, m_S} = \langle I, m_I; \ S, m_S | F, m_F \rangle. \tag{47}$$

Each Clebsch-Gordan coefficient is specified by 6 numbers: the total spin of the coupled state F, its projection m_F and the
615 total spins of the uncoupled states and their projections (I, S, m_I, m_S). Coefficient $C^{F, m_F}_{I, m_I, S, m_S}$ represents "how much" of uncoupled state $|I, m_I, S, m_S\rangle$ there is in a coupled state $|F, m_F\rangle$. The analytical values of the Clebsch-Gordan coefficients can be calculated using recursive expressions, and are available in many software packages and textbooks. Table 1 in the Supplementary Material provides the relation between the coupled and uncoupled states for the considered A_3 system and shows explicitly how to calculate them. The full set of all possible $|F, m_F\rangle$ states forms the new basis that is better suited
620 than the Zeeman basis for ZULF NMR. In fact, this basis coincides with the eigenstates at ZULF for A_n and for XA_n systems, but this basis is also a good starting point for more complicated cases. We will refer to this new basis as to "coupled" basis because it is appropriate for the description of strongly coupled spins.

4.2 Eigenenergies at zero-field

Having the eigenstates, we can now proceed with finding the eigenvalues of the Hamiltonian; these values correspond to the
625 energy of the state and therefore determine the frequencies of ZULF NMR transitions. It turns out that A_n systems are not detectable at ZULF; it is shown in the next section (where intensities of transitions are calculated) that they give rise to no observable transition. At least two types of nuclei with different gyromagnetic ratios are necessary for an observable

transition to exist. Therefore, we consider an XA$_n$ system from now on. We will denote the operators associated with the X spin as $\hat{S}$ and with A spins as $\hat{I}$. The Hamiltonian at ZF for this spin system is given by

630   $\hat{H}_{AX} = 2\pi J_{AX} \sum_{a=1}^{n} \hat{\mathbf{S}} \cdot \hat{\mathbf{I}}_a + 2\pi J_{AA} \sum_{a=1}^{n-1} \sum_{b>a}^{n} \hat{\mathbf{I}}_a \cdot \hat{\mathbf{I}}_b.$ (48)

The $\hat{H}_{AX}$ Hamiltonian can be expressed in terms of the total spin operators using algebraic tricks. We find an expression for the first term of (48) in terms of $\hat{F}^2$, $\hat{I}^2$ and $\hat{S}^2$ by developing $\hat{F}^2$

$$\hat{F}^2 = \left(\hat{\mathbf{S}} + \sum_{a=1}^{n} \hat{\mathbf{I}}_a\right)^2 = \hat{S}^2 + 2\hat{\mathbf{S}} \cdot \sum_{a=1}^{n} \hat{\mathbf{I}}_a + \left(\sum_{a=1}^{n} \hat{\mathbf{I}}_a\right)^2 = \hat{S}^2 + 2\sum_{a=1}^{n} \hat{\mathbf{S}} \cdot \hat{\mathbf{I}}_a + \hat{I}^2 \iff$$

$$\sum_{a=1}^{n} \hat{\mathbf{S}} \cdot \hat{\mathbf{I}}_a = \frac{1}{2}\left(\hat{F}^2 - \hat{S}^2 - \hat{I}^2\right).$$ (49)

635   Similarly, we find an expression for the second term of (48) in terms of $\hat{I}^2$ and $\hat{I}_a^2$ by developing $\hat{I}^2$

$$\hat{I}^2 = \left(\sum_{a=1}^{n} \hat{\mathbf{I}}_a\right)^2 = \sum_{a=1}^{n} \hat{I}_a^2 + 2\sum_{a=1}^{n-1} \sum_{b>a}^{n} \hat{\mathbf{I}}_a \cdot \hat{\mathbf{I}}_b \iff$$

$$\sum_{a=1}^{n-1} \sum_{b>a}^{n} \hat{\mathbf{I}}_a \cdot \hat{\mathbf{I}}_b = \frac{1}{2}\left(\hat{I}^2 - \sum_{a=1}^{n} \hat{I}_a^2\right).$$ (50)

By substituting the results of (49) and (50) into (48), we obtain a form of the Hamiltonian for which the energies will be more easily calculated

640   $\hat{H}_{AX} = 2\pi J_{AX} \frac{1}{2}\left(\hat{F}^2 - \hat{S}^2 - \hat{I}^2\right) + 2\pi J_{AA} \frac{1}{2}\left(\hat{I}^2 - \sum_{a=1}^{n} \hat{I}_a^2\right).$ (51)

The $\hat{H}_{AX}$ Hamiltonian commutes with the $\hat{F}^2$ operator, and therefore they share eigenstates $|F, m_F\rangle$. So, the eigenenergies can be written as the expectation values of $|F, m_F\rangle$ with respect to $\hat{H}_{AX}$

$E_{F,m_F} = \langle F, m_F | \hat{H}_{AX} | F, m_F \rangle.$ (52)

To calculate explicitly the eigenvalues, we substitute the Hamiltonian of (51) into (52) and use the following properties

645   $\begin{aligned} \hat{F}^2 |F, m_F\rangle &= F(F+1)|F, m_F\rangle \\ \hat{S}^2 |F, m_F\rangle &= S(S+1)|F, m_F\rangle \\ \hat{I}^2 |F, m_F\rangle &= I(I+1)|F, m_F\rangle \\ \hat{I}_a^2 |F, m_F\rangle &= I_a(I_a+1)|F, m_F\rangle \end{aligned}$,   (53)

to obtain the final expression for the energy of level $|F, m_F\rangle$

$$E_{F,mF} = \frac{J_{AX}}{2}[F(F+1) - S(S+1) - I(I+1)] + \frac{J_{AA}}{2}[I(I+1) - nI_a(I_a+1)],\qquad(54)$$

650 expressed in Hz. Here, quantum number F corresponds to the total spin of the full XA_n system, S corresponds to the spin of the nucleus X, I is the total spin of the A_n spins, and I_a is the spin of individual nuclei A.

The spin S is the same for all eigenstates (e.g. it is ½ for ^{13}C); similarly, all spins I_a are the same and for ^1H spins they are equal to ½. The remaining two quantum numbers F and S can have different values depending on the state, therefore removing degeneracy between some of the levels. Figure 8 presents the energy levels of XA, XA_2, and XA_3 systems at ZF

655 calculated using (54).
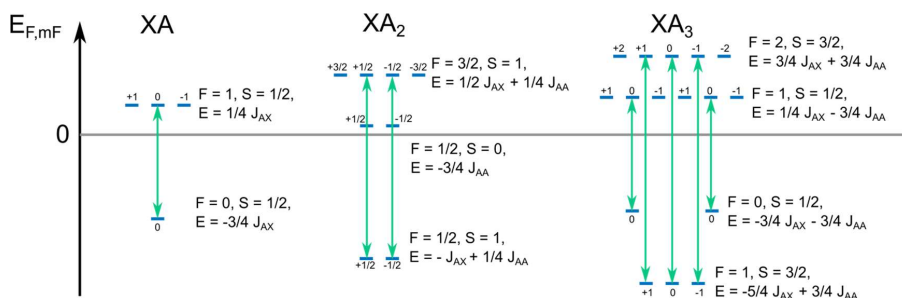
Figure 8: Energy levels for XA, XA_2, and XA_3 spin systems calculated according to (54). The numbers above the energy levels represent the z-projection of the angular momentum of the states m_F. Allowed transitions are shown by green arrows. J_{AX} was set
660 **to 140 Hz and J_{AA} was set to -12 Hz, these are typical values for $1J_{CH}$ and $2J_{HH}$ J-couplings. The energy difference for the allowed transitions equals to J_{AX} for the XA system, $3/2J_{AX}$ for the XA_2 system, and two frequencies of $2J_{AX}$ and of J_{AX} for the XA_3 system. This agrees with the numerical simulations shown in Figure 6.**

4.3 Selection rules

We have now found the eigenstates and their energies but not all transitions between any pair of states are allowed. The last
665 step is to find the transition intensities and thus get the analytical appearance for the ZF NMR spectrum of an XAn system. There are certain selection rules specifying which transitions are in principle possible and which are forbidden, like those in high-field NMR, where only single quantum transitions are allowed. A general expression for the transition intensity between any two eigenstates $|F, m_F\rangle$ and $|F', m'_F\rangle$ is given by

$$Y = \langle F', m'_F|\hat{\rho}_0|F, m_F\rangle\langle F', m'_F|\hat{O}|F, m_F\rangle.\qquad(55)$$

670 We will explicitly calculate the transition intensity for the sudden field drop experiment. In this case, both the initial state $\hat{\rho}_0$ and the observation operator $\hat{O}$ are proportional to $\gamma_I\hat{I}_z + \gamma_S\hat{S}_z$. Therefore, the transition intensity becomes

$$Y = \langle F', m'_F|\gamma_I\hat{I}_z + \gamma_S\hat{S}_z|F, m_F\rangle^2.\qquad(56)$$

This expression is an example of Fermi's golden rule that is used to calculate transition's amplitude in different problems on quantum mechanics. Similar expression can be found for the high-field NMR. By expressing the coupled states $|F, m_F\rangle$ in terms of uncoupled basis (see (46)) we find that

$$\left(\gamma_I \hat{I}_z + \gamma_S \hat{S}_z\right)|F, m_F\rangle = \left(\gamma_I \hat{I}_z + \gamma_S \hat{S}_z\right) \sum_{m_I, m_S} C_{I,m_I,S,m_S}^{F,m_F} |I, m_I, S, m_S\rangle$$

$$= \sum_{m_I, m_S} C_{I,m_I,S,m_S}^{F,m_F} (\gamma_I m_I + \gamma_S m_S)|I, m_I, S, m_S\rangle, \tag{57}$$

where m_I and m_S are the z-projection of spin I and S, respectively. Now let us express the remaining $\langle F', m'_F|$ state in terms of uncoupled basis as well and combine (56) and (57)

$$Y = \left(\sum_{m'_I, m'_S} C_{I',m'_I,S',m'_S}^{F',m'_F} \langle I', m'_I, S', m'_S| \sum_{m_I, m_S} C_{I,m_I,S,m_S}^{F,m_F} (\gamma_I m_I + \gamma_S m_S) |I, m_I, S, m_S\rangle\right)^2$$

$$= \left(\sum_{m'_I, m'_S, m_I, m_S} C_{I',m'_I,S',m'_S}^{F',m'_F} C_{I,m_I,S,m_S}^{F,m_F} (\gamma_I m_I + \gamma_S m_S)\langle I', m'_I, S', m'_S|I, m_I, S, m_S\rangle\right)^2 \tag{58}$$

The last term $\langle I', m'_I, S', m'_S|I, m_I, S, m_S\rangle$ is nonzero only if

$$\begin{aligned} \Delta I &= I' - I = 0 \\ \Delta m_I &= m_I' - m_I = 0 \\ \Delta S &= S' - S = 0 \\ \Delta m_S &= m_S' - m_S = 0 \end{aligned}. \tag{59}$$

These selection rules mean that the only allowed transition are those which conserve the total spins I and S, as well as their projections onto the reference axis. (68) therefore simplifies to

$$Y = \left(\sum_{m_I, m_S} C_{I,m_I,S,m_S}^{F',m'_F} C_{I,m_I,S,m_S}^{F,m_F} (\gamma_I m_I + \gamma_S m_S)\right)^2. \tag{60}$$

It is important to notice that, in case where $\gamma_I = \gamma_S$, each element of this sum becomes antisymmetric with respect to change of the sign of the projections $m_I \in \{-I, -I + 1, \dots, I + 1, I\}$ and $m_S \in \{-S, -S + 1, \dots, S + 1, S\}$

$$C_{I,m_I,S,m_S}^{F',m'_F} C_{I,m_I,S,m_S}^{F,m_F} 2\gamma m_I = -C_{I,m_I,S,m_S}^{F',m'_F} C_{I,m_I,S,m_S}^{F,m_F} 2\gamma(-m_I). \tag{61}$$

This antisymmetry leads to the fact that, for $\gamma = \gamma_I = \gamma_S$, the intensities of all possible transitions are always zero, which explains why ZULF NMR J-spectroscopy requires having at least two types of nuclei.

Finally, there are two more selection rules that are derived by implementing Wigner–Eckart theorem. The considered case is equivalent to "dipole" transition, where the transition is observed between two states connected by operator of rank 1 (e.g. (56)). This is a common situation in atomic physics, and we adapt this result without evaluation: the reduced matrix element coming from Wigner–Eckart is shown to be non-zero if and only if

$$\Delta F = \pm 1$$
$$\Delta m_F = 0.$$

(62)

The whole set of selection rules given by (59) and (62) allows us to find which transitions are observable in XA_n systems at ZF. These transitions are shown in Figure 8 by the green arrows. It can be seen that J_{AA}-couplings shift the energy levels but do not affect the frequencies of the observable transitions. This is a common situation that J-couplings between magnetically

700 equivalent spins do not contribute to the observed NMR spectrum. As can be seen from the analysis presented above, this statement holds for each case of the ZF NMR spectra of XA_n systems.

In this section, we found analytically the allowed transitions for XA, XA_2 and XA_3 for the case of sudden field drop to ZF. The XA spin system has a single transition at J_{AX}; The XA_2 spin system has a single transition at $3/2\ J_{AX}$; and the XA_3 spin system has one allowed transition at J_{AX} and another one at $2\ J_{AX}$. Allowed transitions found analytically here correspond to

705 the numerical simulation: XA single line at J_{AX}, XA_2 single line at $3/2\ J_{AX}$, etc.. This derivation explained the appearance of the ZF spectra but not that of the ultralow-field spectra. To understand how the degeneracy of the ZF eigenstates are split by the presence of a bias field, one has to use perturbation theory. We refer the interested reader to Refs (Ledbetter et al., 2011; Appelt et al., 2010).

5 Conclusion

710 We have shown how to numerically simulate spectra at both zero- and ultra-low fields for sudden drop and pulsed experiments. We have then explained the results of the numerical simulation for sudden drop experiments at ZF by constructing the eigenbasis of the ZF Hamiltonian and finding the allowed transitions among the eigenstates. The other numerically simulated cases (i.e. pulsed experiments) can be explained using the analytical approach that we have presented here. It requires an additional step which is to describe how a pulse converts the populations of states. The reader who is

715 acquainted with the product operator formalism commonly used in high-field NMR might be interested in an alternative approach based of commutation rules as presented in Refs (Blanchard and Budker, 2016; Butler et al., 2013b). We have chosen to describe the simplest case, i. e., experiments with thermal prepolarization. The formalism we presented here is a good starting point for the description and understanding of hyperpolarized ZULF experiments. It can also be used to simulate the transition between the ZULF and high-field regime (Bodenstedt et al., 2021). We hope that this Tutorial Paper

720 has allowed us to share our excitement with the reader.

Code availability

The codes used to simulate the spectra presented in this Paper are available online (https://doi.org/10.5281/zenodo.7271319). PDF versions of the codes are available as Supplementary Material to the Paper.

Acknowledgements

725 This research was supported by ENS-Lyon, the French CNRS, Lyon 1 University, the European Research Council under the European Union's Horizon 2020 research and innovation program (Marie Sklodowska-Curie grant agreement no. 766402/ZULF), and the French National Research Agency (project 'HyMag' ANR-18-CE09-0013).

References

Appelt, S., Häsing, F. W., Sieling, U., Gordji-Nejad, A., Glöggler, S., and Blümich, B.: Paths from weak to strong coupling
730 in NMR, Phys. Rev. A, 81, 023420, https://doi.org/10.1103/PhysRevA.81.023420, 2010.

Barskiy, D. A., Tayler, M. C. D., Marco-Rius, I., Kurhanewicz, J., Vigneron, D. B., Cikrikci, S., Aydogdu, A., Reh, M., Pravdivtsev, A. N., Hövener, J.-B., Blanchard, J. W., Wu, T., Budker, D., and Pines, A.: Zero-field nuclear magnetic resonance of chemically exchanging systems, Nat Commun, 10, 3002, https://doi.org/10.1038/s41467-019-10787-9, 2019.

Bengs, C. and Levitt, M. H.: SpinDynamica: Symbolic and numerical magnetic resonance in a Mathematica environment,
735 Magnetic Resonance in Chemistry, 56, 374–414, https://doi.org/10.1002/mrc.4642, 2018.

Blanchard, J. W. and Budker, D.: Zero- to Ultralow-Field NMR, in: eMagRes, John Wiley & Sons, Ltd, 1395–1410, https://doi.org/10.1002/9780470034590.emrstm1369, 2016.

Blanchard, J. W., Sjolander, T. F., King, J. P., Ledbetter, M. P., Levine, E. H., Bajaj, V. S., Budker, D., and Pines, A.: Measurement of untruncated nuclear spin interactions via zero- to ultralow-field nuclear magnetic resonance, Phys. Rev. B,
740 92, 220202, https://doi.org/10.1103/PhysRevB.92.220202, 2015.

Blanchard, J. W., Wu, T., Eills, J., Hu, Y., and Budker, D.: Zero- to ultralow-field nuclear magnetic resonance J-spectroscopy with commercial atomic magnetometers, Journal of Magnetic Resonance, 314, 106723, https://doi.org/10.1016/j.jmr.2020.106723, 2020.

Blanchard, J. W., Budker, D., and Trabesinger, A.: Lower than low: Perspectives on zero- to ultralow-field nuclear magnetic
745 resonance, Journal of Magnetic Resonance, 323, 106886, https://doi.org/10.1016/j.jmr.2020.106886, 2021.

Bodenstedt, S., Mitchell, M. W., and Tayler, M. C.: Fast-field-cycling ultralow-field nuclear magnetic relaxation dispersion, Nature Communications, 12, 1–8, 2021.

Butler, M. C., Ledbetter, M. P., Theis, T., Blanchard, J. W., Budker, D., and Pines, A.: Multiplets at zero magnetic field: The geometry of zero-field NMR, The Journal of Chemical Physics, 138, 184202, https://doi.org/10.1063/1.4803144, 2013a.

750 Butler, M. C., Kervern, G., Theis, T., Ledbetter, M. P., Ganssle, P. J., Blanchard, J. W., Budker, D., and Pines, A.: Parahydrogen-induced polarization at zero magnetic field, The Journal of Chemical Physics, 138, 234201, https://doi.org/10.1063/1.4805062, 2013b.

Emondts, M., Ledbetter, M. P., Pustelny, S., Theis, T., Patton, B., Blanchard, J. W., Butler, M. C., Budker, D., and Pines, A.: Long-Lived Heteronuclear Spin-Singlet States in Liquids at a Zero Magnetic field, Phys. Rev. Lett., 112, 077601,
755 https://doi.org/10.1103/PhysRevLett.112.077601, 2014.

NaNNaNNaNNaNNaNNaNNaNNaNNaNNaN

NaNNaNNaNNaNNaN
NaNNaN
NaNNaNNaN
NaNNaN

NaN
NaN
NaN
NaNNaNNaN
NaN
NaNNaN
NaN
NaNNaN
NaNNaN
NaN
NaNNaNNaN

NaNNaN
NaNNaN
NaN
NaNNaN

Hogben, H. J., Krzystyniak, M., Charnock, G. T. P., Hore, P. J., and Kuprov, I.: Spinach – A software library for simulation of spin dynamics in large spin systems, Journal of Magnetic Resonance, 208, 179–194, https://doi.org/10.1016/j.jmr.2010.11.008, 2011.

Hore, P. J., Jones, J. A., and Wimperis, S.: NMR: The Toolkit : how Pulse Sequences Work, Oxford University Press, 133 pp., 2015.

Ledbetter, M. P., Crawford, C. W., Pines, A., Wemmer, D. E., Knappe, S., Kitching, J., and Budker, D.: Optical detection of NMR J-spectra at zero magnetic field, Journal of Magnetic Resonance, 199, 25–29, https://doi.org/10.1016/j.jmr.2009.03.008, 2009.

Ledbetter, M. P., Theis, T., Blanchard, J. W., Ring, H., Ganssle, P., Appelt, S., Blümich, B., Pines, A., and Budker, D.: Near-Zero-Field Nuclear Magnetic Resonance, Phys. Rev. Lett., 107, 107601, https://doi.org/10.1103/PhysRevLett.107.107601, 2011.

Levitt, M. H.: Spin Dynamics: Basics of Nuclear Magnetic Resonance, John Wiley & Sons, 885 pp., 2013.

Otting, G., Widmer, H., Wagner, G., and Wüthrich, K.: Origin of t2 and t2 ridges in 2D NMR spectra and procedures for suppression, Journal of Magnetic Resonance, 66, 187–193, https://doi.org/10.1016/0022-2364(86)90122-8, 1986.

Put, P., Pustelny, S., Budker, D., Druga, E., Sjolander, T. F., Pines, A., and Barskiy, D. A.: Zero- to Ultralow-Field NMR Spectroscopy of Small Biomolecules, Anal. Chem., 93, 3226–3232, https://doi.org/10.1021/acs.analchem.0c04738, 2021.

Schwalbe, H.: Editorial: New 1.2 GHz NMR Spectrometers— New Horizons?, Angewandte Chemie International Edition, 56, 10252–10253, https://doi.org/10.1002/anie.201705936, 2017.

Tayler, M. C. D., Theis, T., Sjolander, T. F., Blanchard, J. W., Kentner, A., Pustelny, S., Pines, A., and Budker, D.: Invited Review Article: Instrumentation for nuclear magnetic resonance in zero and ultralow magnetic field, Review of Scientific Instruments, 88, 091101, https://doi.org/10.1063/1.5003347, 2017.

Thayer, A. M. and Pines, A.: Zero-field NMR, Accounts of Chemical Research, 20, 47–53, 1987.

Theis, T., Ledbetter, M. P., Kervern, G., Blanchard, J. W., Ganssle, P. J., Butler, M. C., Shin, H. D., Budker, D., and Pines, A.: Zero-Field NMR Enhanced by Parahydrogen in Reversible Exchange, J. Am. Chem. Soc., 134, 3987–3990, https://doi.org/10.1021/ja2112405, 2012.

Theis, T., Blanchard, J. W., Butler, M. C., Ledbetter, M. P., Budker, D., and Pines, A.: Chemical analysis using J-coupling multiplets in zero-field NMR, Chemical Physics Letters, 580, 160–165, https://doi.org/10.1016/j.cplett.2013.06.042, 2013.

Weitekamp, D. P., Bielecki, A., Zax, D., Zilm, K., and Pines, A.: Zero-Field Nuclear Magnetic Resonance, Phys. Rev. Lett., 50, 1807–1810, https://doi.org/10.1103/PhysRevLett.50.1807, 1983.

Yurkovskaya, A. and Bodenhausen, G.: In memoriam Konstantin L'vovich Ivanov, Magnetic Resonance, 2, 341–342, https://doi.org/10.5194/mr-2-341-2021, 2021.

Zhu, G., Torchia, D. A., and Bax, A.: Discrete Fourier Transformation of NMR Signals. The Relationship between Sampling Delay Time and Spectral Baseline, Journal of Magnetic Resonance, Series A, 105, 219–222, https://doi.org/10.1006/jmra.1993.1274, 1993.